

NIR SPECTROSCOPIC OBSERVATION OF MASSIVE GALAXIES IN THE PROTOCLUSTER AT $Z = 3.09$

MARIKO KUBO^{1, 2}, TORU YAMADA², TAKASHI ICHIKAWA², MASARU KAJISAWA³, YUICHI MATSUDA^{4, 5}, ICHI TANAKA⁶

Draft version November 11, 2014

ABSTRACT

We present the results of near-infrared spectroscopic observations of the K -band selected candidate galaxies in the protocluster at $z = 3.09$ in the SSA22 field. We observed 67 candidates with $K_{AB} < 24$ and confirmed redshifts of the 39 galaxies at $2.0 < z_{\text{spec}} < 3.4$. Of the 67 candidates, 24 are certainly protocluster members with $3.04 \leq z_{\text{spec}} \leq 3.12$, which are massive red galaxies those have been unidentified in previous optical observations of the SSA22 protocluster. Many distant red galaxies (DRGs; $J - K_{AB} > 1.4$), hyper extremely red objects (HEROs; $J - K_{AB} > 2.1$), *Spitzer* MIPS 24 μm sources, active galactic nuclei (AGNs) as well as the counterparts of Ly α blobs and the AzTEC/ASTE 1.1-mm sources in the SSA22 field are also found to be the protocluster members. The mass of the SSA22 protocluster is estimated to be $\sim 2 - 5 \times 10^{14} M_{\odot}$ and this system is plausibly a progenitor of the most massive clusters of galaxies in the current Universe. The reddest ($J - K_{AB} \geq 2.4$) protocluster galaxies are massive galaxies with $M_{\text{star}} \sim 10^{11} M_{\odot}$ showing quiescent star formation activities and plausibly dominated by old stellar populations. Most of these massive quiescent galaxies host moderately luminous AGNs detected by X-ray. There are no significant differences in the [OIII] $\lambda 5007/\text{H}\beta$ emission line ratios, and [OIII] $\lambda 5007$ line widths and spatial extents of the protocluster galaxies from those of massive galaxies at $z \sim 2 - 3$ in the general field.

Subject headings: galaxies: formation — galaxies: high-redshift — galaxies: evolution — cosmology: observations — galaxies: clusters

1. INTRODUCTION

Clusters of galaxies are good evolutionary probes for determining the structure formation history in the Universe. Number density of massive clusters at given redshift is an important quantity for constraining the structure formation model as well as the cosmological parameters. It is reported that dynamically relaxed, mature clusters already existed at $z \sim 1.5 - 2$ (e.g., Mullis et al. 2005; Gobat et al. 2011; Fassbender et al. 2011). At $z > 2$, a number of protoclusters were discovered (e.g., Steidel et al. 1998; Venemans et al. 2005; Ouchi et al. 2005; Matsuda et al. 2011; Toshikawa et al. 2012) although their structures, dynamical properties and masses have yet to be revealed well. Masses of protoclusters can be measured based on e.g., their velocity dispersions and overdensities, (e.g., Venemans et al. 2005) but require spectroscopic redshift constraints enough to disclose their galaxy distributions.

On the other hand, protoclusters are suitable targets for studying the formation history of massive early-type galaxies those dominate cores of massive clusters in the current Universe. There is a well-established color-magnitude relation among massive early-type galaxies in local clusters (e.g., Visvanathan & Sandage 1977; Bower

et al. 1992), and also in clusters at out to $z \sim 1$ (e.g., Ellis et al. 1997; Stanford et al. 1998). The tight color-magnitude relation implies that the bulk of the stars in massive early-type galaxies formed at $z > 2$. Density excesses of massive red galaxies in protoclusters at $z = 2 - 3$ (e.g., Kodama et al. 2007; Uchimoto et al. 2012) also suggest that massive early-type galaxies began to assemble at as early as $z = 2 - 3$. In the meanwhile, massive quiescent galaxies at out to $z \sim 5$ were found from field surveys based on color selections (e.g., Caputi et al. 2012; Ilbert et al. 2013; Muzzin et al. 2013; Straatman et al. 2014) and also confirmed at out to $z \sim 3$ (Gobat et al. 2012; Marsan et al. 2014). But the relationship between such high- z analogues and massive early-type galaxies in local clusters remains unclear.

The protocluster at $z = 3.09$ in the SSA22 field is known as one of the most outstanding structures at high redshift. This protocluster was characterized by the significant over-densities of Lyman-break galaxies (LBGs) and Ly α emitters (LAEs) at $z \approx 3.09$ associated with the superstructure extended over ~ 100 Mpc (Steidel et al. 1998, 2000; Hayashino et al. 2004; Yamada et al. 2012). The density excesses of Ly α blobs (LABs; Matsuda et al. 2004), the AzTEC/ASTE 1.1-mm sources (Tamura et al. 2009; Umehata et al. 2014) and active galactic nuclei (AGNs) (Lehmer et al. 2009b), which may associate with the massive galaxy formation were also reported.

We have studied massive red galaxies in the SSA22 protocluster by using our own deep and wide near-infrared (NIR) imaging data taken with Multi-Objects Infra-Red Camera and Spectrograph (MOIRCS) equipped with Subaru Telescope ($K \approx 24$ at 5σ for 111.8 arcmin², Uchimoto et al. 2008, 2012; Kubo et al. 2013). We found the surface number density excesses of distant red galaxies (DRGs, $J - K > 1.4$; Franx et al. 2003), hyper

¹ Institute for Cosmic Ray Research, University of Tokyo, 5-1-5 Kashiwa-no-Ha, Kashiwa City Chiba, 277-8582, Japan

² Astronomical Institute, Tohoku University, 6-3 Aoba, Aramaki, Aoba-ku, Sendai, Miyagi, 980-8578, Japan

³ Research Center for Space and Cosmic Evolution, Ehime University, Bunkyo-cho 2-5, Matsuyama 790-8577, Japan

⁴ Chile Observatory, National Astronomical Observatory of Japan, Tokyo 181-8588, Japan

⁵ Graduate University for Advanced Studies (SOKENDAI), Osawa 2-21-1, Mitaka, Tokyo 181-8588, Japan

⁶ Subaru Telescope, National Astronomical Observatory of Japan, 650 North A !ohoku Place, Hilo, HI 96720, USA

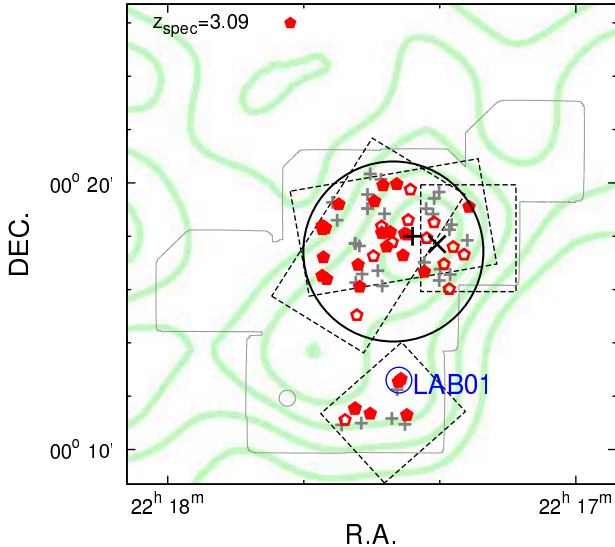


Figure 1. Sky coordinates of the targets. The boxes with black dashed lines show the locations of the slit masks for our NIR spectroscopy. The filled red pentagons show the galaxies confirmed at $3.04 \leq z_{\text{spec}} \leq 3.12$ and the blank red pentagons show those at $z_{\text{spec}} < 3.04$ or $z_{\text{spec}} > 3.12$. The gray crosses show the targets observed but unidentified their redshifts. We use the targets within the black large circle with 1.5 Mpc radius in physical scale (≈ 3.3 arcmin) to estimate the cluster mass in § 4. 1. The gray solid lines enclose the FoV of the MOIRCS K -band images (Uchimoto et al. 2012). The green contours show the surface density levels of LAEs at $z = 3.09$ and the black large cross shows its peak obtained by Yamada et al. (2012). The black large X shows the density peak of the K -selected galaxies at $2.6 < z_{\text{phot}} < 3.6$ obtained by Kubo et al. (2013). The blue large circle indicates the location of LAB01 (Steidel et al. 2000).

extremely red objects (HEROs, $J - K > 2.1$; Totani et al. 2001) as well as galaxies with photometric redshift $2.6 < z_{\text{phot}} < 3.6$, and those detected with *Chandra* and *Spitzer* MIPS $24 \mu\text{m}$ suggesting enhanced AGN and star formation activities. On the other hand, up to 50% of the galaxies with stellar mass $M_{\text{star}} > 10^{11} M_{\odot}$ at $2.6 < z_{\text{phot}} < 3.6$ in this field have spectral energy distributions (SEDs) dominated by old stellar populations.

Here we present the results of NIR spectroscopy for the K -band selected (K -selected) candidates of the galaxies in the SSA22 protocluster. Our objectives are to confirm the overdensity of the K -selected galaxies in the SSA22 protocluster, investigate their nature and estimate the mass of the SSA22 protocluster itself to disclose the formation and evolutionary history of massive clusters and massive galaxies inside clusters. The K -selected galaxies are massive galaxies which should be hosted in massive halos. Therefore, they are excellent tracers of cluster mass and also very plausible progenitors of massive early-type galaxies. Since our targets are faint in rest-frame UV, nebular emission lines at rest-frame optical are the most useful probes to confirm their redshifts. In this paper, we assume cosmological parameters of $H_0 = 70 \text{ km s}^{-1} \text{ Mpc}^{-1}$, $\Omega_m = 0.3$ and $\Omega_{\Lambda} = 0.7$. We use the AB magnitude system throughout this paper.

2. OBSERVATIONS AND DATA REDUCTIONS

The observations were conducted with MOIRCS on Subaru Telescope during 2012 September 29-30 and October 27-28. Summary of the observations is given in Table 1. We used the Multi-Object Spectroscopy (MOS) mode of MOIRCS. The locations of the MOS slit masks and the targets are shown in Figure 1. Our targets were the candidate members of the SSA22 protocluster with $K < 24$ and $2.6 < z_{\text{phot}} < 3.6$, selected based on the photometric redshifts obtained by Uchimoto et al. (2012) and Kubo et al. (2013). We used the four MOS slit masks to cover the density peaks of LAEs at $z \approx 3.09$ (Yamada et al. 2012) and the K -selected galaxies at $2.6 < z_{\text{phot}} < 3.6$ (Kubo et al. 2013) and also LAB01, which is known as one of the largest LABs (Steidel et al. 2000). In total, we observed 67 objects while four of them were observed twice with the different slit masks.

We put priority on DRGs, HEROs, *Spitzer* MIPS $24 \mu\text{m}$ sources, *Chandra* X-ray sources, and the counterparts of LABs and the AzTEC/ASTE 1.1-mm sources (selected based on Matsuda et al. 2004; Webb et al. 2009; Lehmer et al. 2009b; Umehata et al. 2014). The numbers of the targets satisfying each classification are listed in Table 2. The detection limit of the *Chandra* data corresponds to $L_X \sim 10^{43} \text{ erg s}^{-1}$. The objects with flux in MIPS $24 \mu\text{m}$ -band $f_{24\mu\text{m}} \gtrsim 60 \mu\text{Jy}$ are identified as $24 \mu\text{m}$ sources. Such luminous mid-infrared sources at $z > 2$ are not likely to be only originated in dusty starburst but also obscured AGNs (e.g., Daddi et al. 2007). Actually, of the 18 targets detected at $24 \mu\text{m}$, four are also detected with *Chandra*. Some of DRGs, $24 \mu\text{m}$ and X-ray sources were selected as the targets regardless of their photometric redshifts.

MOIRCS consists of two channels, Ch1 and Ch2, with each $3'.5 \times 4'.0$ field of view (FoV). We used the Volume Phase Holographic K -band grism for Ch2 (VPH- K ; Ebizuka et al. 2011). The VPH- K grism covers a wavelength range from 1.9 to $2.3 \mu\text{m}$ with $R \sim 1700$ with $0''.8$ slit width. For Ch1, we had to use the *HK500* grism due to the instrument trouble occurred during the run. The *HK500* grism covers a wavelength range from 1.3 to $2.3 \mu\text{m}$ with $R \sim 500$ with $0''.8$ slit width. Ch1 could not be used for the mask alignments for the first two nights. The total exposure time was 3.6 – 4.4 hours for each mask. The seeing size in the K_s -band during the observations was typically $0''.6$, ranging from $0''.4$ to $0''.8$. The telescope was dithered along the slits by $3''.0$ for sky subtractions. Flux standard stars for the VPH- K grism were taken at the ends of the observations using the slits in the object masks. The flux values were calibrated to their K -band total magnitudes given in Two Micron All Sky Survey point source catalog (Skrutskie et al. 2006). Since acquisitions of known standard stars were not available for Ch1 during the run, the bright stars in the object masks were used for the calibration.

The data reduction was performed by using IRAF scripts for Subaru/MOIRCS MOS data (MCSMDP¹) following its standard manner (e.g., Yoshikawa et al. 2010). Note that, the order-sorting filter was not used during the observations on September 29 and 30 and we corrected the contributions of the second order spectra. The error from this procedure is 0.4 – 0.7% of a flux value.

The *HK500* grism provides a spectral resolution of

¹ available at <http://www.naoj.org/Observing/DataReduction/>

Table 1
Summary of the observation

mask ID	R.A. (J2000.0)	Dec (J2000.0)	P.A. ^a (degree)	UT date	exposure (sec)	seeing ^b (arcsec)	channel	grism	target (number)
SSA22B	22 17 31.7	00 12 40.7	222	2012 Sep 29	14000	0.6	Ch1	VPH-K	... ^c
							Ch2	VPH-K	12
SSA22A1	22 17 22.6	00 17 55.1	270	2012 Sep 30	16000	0.7	Ch1	VPH-K	... ^c
							Ch2	VPH-K	12
SSA22D	22 17 26.8	00 18 19.4	280	2012 Oct 27	13000	0.4	Ch1	HK500	13
							Ch2	VPH-K	10
SSA22C	22 17 30.5	00 17 39.8	148	2012 Oct 28	13600	0.5	Ch1	HK500	11
							Ch2	VPH-K	13

^aDirections of the slits, from north to east

^bAverage PSF sizes in the K_s -band during the observations

^cCh1 did not work during the observations on September 29 and 30.

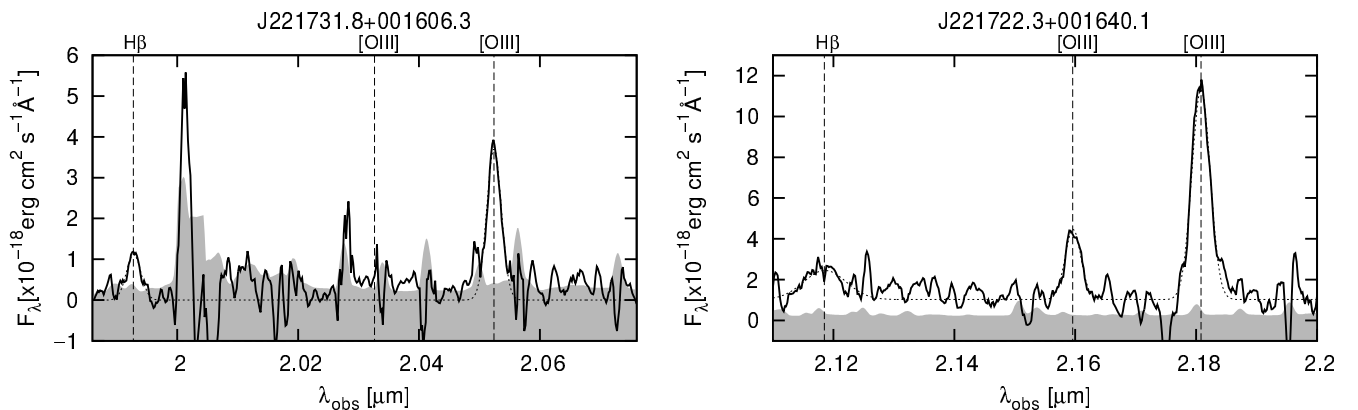


Figure 2. The K -band spectra of J221731.8+001606.3 at $z_{\text{spec}} = 3.0981$ (left) and J221722.3+001640.1 at $z_{\text{spec}} = 3.3544$ (right). The black solid lines show the obtained spectra and the gray shaded areas show 1σ Poisson noise of the sky background. The dotted curves show the best-fit line profiles obtained by using the SPECFIT. The dashed vertical lines are drawn at the wavelength of [OIII] $\lambda 4959$, 5007 and H β emission lines while the wavelength of [OIII] $\lambda 4959$ of J221731.8+001606.3 is shown at that expected from its [OIII] $\lambda 5007$ but obscured by OH airglow lines.

40\AA with $0''.8$ slit while the VPH- K grism provides spectral resolutions of 9\AA and 11\AA with $0''.7$ slit and $0''.8$ slit, respectively. Spectral coverages of the VPH- K and HK500 grism correspond to the redshifted [OIII] $\lambda 5007$ emission line at $2.9 < z < 3.6$ and $1.9 < z < 3.6$, respectively, excluding $2.7 < z < 2.9$ where spectra are buried by strong atmospheric absorption. Efficiency of the VPH- K grism is the highest at $\sim 2.05\ \mu\text{m}$, where [OIII] $\lambda 5007$ at $z \approx 3.09$ is shifted to. It basically depends on wavelength and location of a slit in the direction of dispersion but is almost uniform for our slit arrangements. Since crowded OH airglow lines are well-resolved, S/N ratios of the spectra obtained by using the VPH- K grism are typically higher than those obtained by using the HK500 grism at $\sim 2.05\ \mu\text{m}$.

Figure 2 show examples of the obtained spectra. The flux errors are 1σ Poisson errors of the sky spectra before the sky subtraction at each wavelength. The emission lines were visually identified on the two-dimensional spectra and those with $\sim 1 - 2 \times 10^{-17}\ \text{erg s}^{-1}\ \text{cm}^{-2}$ ($\sim 3\sigma$ of the background noise at $\sim 2.05\ \mu\text{m}$) were detectable. The dotted curve in each panel shows the best-

fit line profile. The one-dimensional profiles of the spectra were inspected after combined the spectra within the appropriate apertures along the slit giving the largest S/N ratios for the detected emission lines. We used the SPECFIT in IRAF (Kris 1994) to measure the flux values, central wavelengths and line width of the detected emission lines by fitting the multiple emission lines and continuum emission simultaneously. Emission lines were fitted with Gaussian profiles while continuum spectra are assumed to be linear functions of wavelength at the fitted regions. The obtained redshifts and flux values are listed in Table 3. The errors of the best-fit profiles are shown as the errors of the redshifts and flux values.

Spectroscopic redshifts are ideally constrained with sets of emission lines but it often happens that only a single emission line is detected due to the sensitivity and obscuration by atmospheric absorption and OH airglow lines. We therefore also consider the redshift probability distribution obtained with the photometric redshift of each galaxy. The uncertainty of our photometric redshift is typically $|z_{\text{spec}} - z_{\text{phot}}| \sim 0.5$ (Kubo et al. 2013), enough accurate to distinguish galaxies at $z \sim 2$, $z \sim 3$

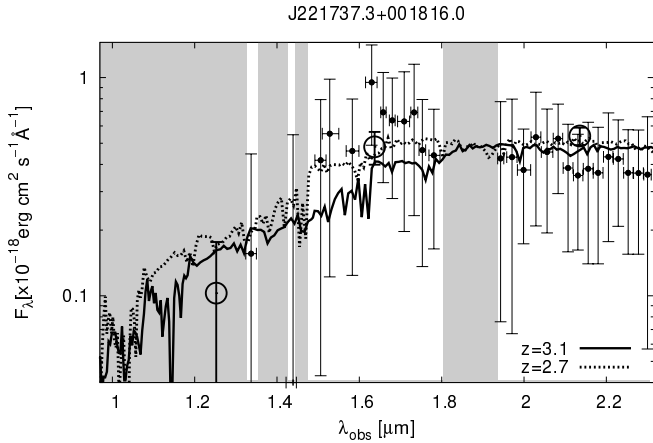


Figure 3. The stacked spectrum of J221737.3+001816.0. The black filled circles show the flux values stacked over the ranges indicated with the horizontal bars. The black large circles show the photometric data points measured on the MOIRCS *JHK*-band images. The black solid curve shows the best-fit SED model obtained with the photometric data, adopting $z = 3.1$ ($\tau = 0.1$, $E(B - V) = 0.1$, age = 2.0 Gyr and $Z = 0.2 Z_{\odot}$) while the full SED is shown in the *top* panel of Figure 6. The black dotted curve shows the best-fit SED model obtained adopting $z = 2.7$ while its SED parameters are same as those obtained adopting $z = 3.1$. The gray shaded areas indicate wavelength ranges obscured by atmospheric absorption and crowded OH airglow lines.

and $z \sim 4$ where the strongest emission lines shifted to $\sim 2 \mu\text{m}$ are $\text{H}\alpha$, $[\text{OIII}] \lambda 5007$ and $[\text{OII}] \lambda 3727$, respectively. We also checked whether the second strongest emission line can be detected as a single line due to the obscuration of the strongest one.

One object, J221737.3+001816.0 is very likely to be at $z \approx 3.09$ from its Balmer and 4000\AA breaks but the solution of $z \sim 2.7$ is also acceptable. Its spectrum is shown in Figure 3. The flux were stacked over the wavelength ranges indicated with the horizontal bar at each point avoiding the wavelength ranges with heavy obscuration by OH airglow lines and atmospheric absorption. There are significant breaks at $\sim 1.4 - 1.5 \mu\text{m}$ and $\sim 1.6 \mu\text{m}$ which are consistent with the Balmer and 4000\AA breaks at $z = 3.0 - 3.15$, respectively. On the other hand, $z \sim 2.7$ is also an acceptable solution where the significant break at $\sim 1.4 - 1.5 \mu\text{m}$ corresponds to 4000\AA break at $z \sim 2.7$. Its whole spectrum is best-fitted with the model with $\tau = 0.1$, $E(B - V) = 0.1$, age = 2.0 Gyr and $Z = 0.2 Z_{\odot}$ at $z \sim 3$ (see also § 4.2) but an offset at 1.5 to 1.8 μm remains. If the offset is not simply due to the photometric errors, additional blue stellar components by small starbursts and minor mergers of bluer systems can be the plausible origins.

3. RESULTS

Table 3 is the list of the 39 galaxies whose redshifts were obtained. Figure 4 shows the redshift distribution of them. Note that it is hard to observe $[\text{OIII}] \lambda 5007$ at $z = 3.00 - 3.03$ and $z = 2.7 - 2.95$ (gray shaded region) due to atmospheric absorption and crowded OH airglow lines. There is a very clear redshift spike at $z \approx 3.09$; Of the 39 galaxies, 24 are at $3.04 \leq z_{\text{spec}} \leq 3.12$, which corresponds to a relative radial velocity of $\pm 3000 \text{ km s}^{-1}$, and considered to be the protocluster members. As

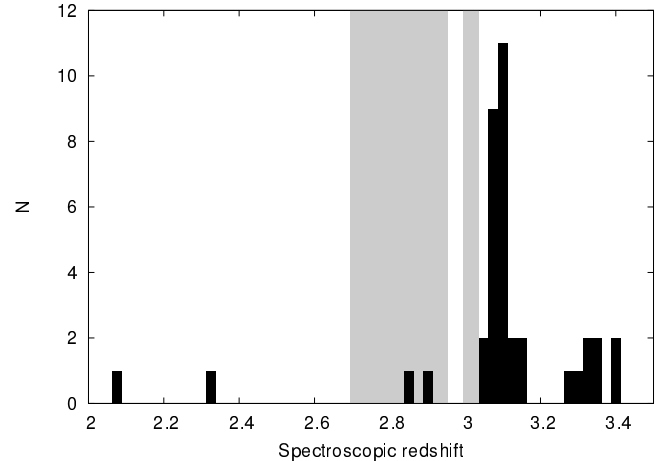


Figure 4. The redshift distribution of the galaxies in the SSA22 field obtained with our NIR spectroscopy. The black histogram shows the redshift distribution of the galaxies confirmed with our NIR spectroscopic observations. The object J221737.3+001816.0 at $z_{\text{spec}} \sim 2.7$, $3.0 - 3.15$ is not included here. At $z > 2.7$, the gray shaded areas indicate redshift ranges where it is hard to confirm redshifts from the redshifted $[\text{OIII}] \lambda 5007$ due to atmospheric absorption and crowded OH airglow lines.

we describe in the next section, the velocity dispersion of the SSA22 protocluster is $\approx 1000 \text{ km s}^{-1}$ and the $\pm 3\sigma$ range is regarded as the cluster members.

Of the 39 galaxies, 11 were known to be at $2.8 < z_{\text{spec}} < 3.4$ from previous optical and NIR spectroscopic observations (Pettini et al. 2001; Steidel et al. 2003; Shapley et al. 2006; Lehmer et al. 2009b; Yamada et al. 2012). Our spectroscopic redshifts agree well with those in literatures while the largest redshift offset is $\Delta z = 0.07$ for J221725.4+001716.9 at $z_{\text{HB}} = 3.0482$ ($z_{\text{lit}} = 3.120$).

Stellar masses of the galaxies were estimated based on the SED fitting of the fluxes in the $u^*BVRI'z'JHK$, 3.6, 4.5, 5.8 and 8.0 μm -bands (Hayashino et al. 2004; Matsuda et al. 2004; Webb et al. 2009; Uchimoto et al. 2012) through a standard χ^2 minimization procedure. The detail of the procedure was described in Kubo et al. (2013). Briefly, we fitted the observed flux values with the Bruzual & Charlot (2003) models with exponentially decay star formation histories where $\text{SFR} \propto \exp(-t/\tau)$ ($\tau = 0.1 - 30 \text{ Gyr}$), metallicity $Z = 0.005, 0.02, 0.2, 0.4, 1 Z_{\odot}$ and the Calzetti et al. (2000) extinction law ranging $E(B - V) = 0.0 - 2.0$. We here adopt the Chabrier Initial Mass Function (IMF) (Chabrier 2003) while we used the Salpeter IMF (Salpeter 1955) in Kubo et al. (2013). Before we perform the SED fittings, we applied slight corrections for the $[\text{OIII}] \lambda 5007$ line fluxes to the K -band fluxes by using the observed values. The errors of the stellar masses show the 68% confidence level of the probability distribution for the stellar mass calculated from a minimum χ^2 value for each object.

Many LBGs and LAEs have already been identified as the members of the SSA22 protocluster with the observations at optical wavelength (Steidel et al. 1998, 2000; Hayashino et al. 2004; Yamada et al. 2012). Our K -band selected and confirmed protocluster galaxies are typically faint in rest-frame UV; only five are detected in the existing Subaru V -band image (Hayashino et al. 2004);

Ly α are detected in the narrow-band image (*NB497*; Hayashino et al. 2004) above 4σ significance for eleven. The median stellar mass of the protocluster galaxies in our sample is $\simeq 5 \times 10^{10} M_{\odot}$ while that of the protocluster DRGs is $\simeq 8 \times 10^{10} M_{\odot}$. The typical stellar mass of LBGs at $z = 2 - 3$ is $\simeq 6 \times 10^9 M_{\odot}$ (mean value; Papovich et al. 2001) and those with $K_s < 22.5$ in Vega ($\lesssim 24.3$ in AB) is $2.5 \times 10^{10} M_{\odot}$ (median value; Shapley et al. 2001), adopting solar metallicity and the Salpeter IMF while stellar mass estimated with the Salpeter IMF is about twice of that estimated with the Chabrier IMF on average (e.g., Erb et al. 2006b; Yoshikawa et al. 2010). From these above, we emphasize that we identified the galaxy population different from those previously found in the SSA22 protocluster.

We summarize the results of the spectroscopy of DRGs, HEROs, $24 \mu\text{m}$ sources, X-ray sources and LAEs (Hayashino et al. 2004) in Table 2. Many of them are certainly the members of the SSA22 protocluster. We also observed the candidate counterparts of the four LABs (Matsuda et al. 2004) and the three AzTEC/ASTE 1.1-mm sources (Umehata et al. 2014). More than one counterparts at $z_{\text{spec}} \approx 3.09$ were identified for each object excluding one 1.1-mm source (AzTEC01 in Umehata et al. 2014). The presence of such multiple counterparts for many LABs and SMGs in the SSA22 field were reported in Uchimoto et al. (2012). They are likely to be the hierarchical multiple mergers at the early-phase of the formation history of massive early-type galaxies, predicted in the cosmological numerical simulations (e.g., Meza et al. 2003; Naab et al. 2007; Oser et al. 2010).

Spatial extents of [OIII] $\lambda 5007$ emission lines $r_{[\text{OIII}]}$ of the galaxies were measured with FWHM of the emission lines along the slits after deconvolved with the PSF profiles. The average values and standard deviations of $r_{[\text{OIII}]}$ of the protocluster galaxies and the field galaxies are 5.0 ± 1.1 kpc and 6.0 ± 1.4 kpc, respectively. Velocity dispersions σ_v of the galaxies were measured for those observed by using the VPH-*K* grism since its instrumental resolution is small enough to resolve kinematics of galaxies with $\sigma_v \gtrsim 70$ km s $^{-1}$. The average and standard deviation of the velocity dispersion of our sample are 137 ± 50 km s $^{-1}$ and 112 ± 51 km s $^{-1}$ for the protocluster galaxies and the field galaxies, respectively, excluding the outliers with $\sigma_v > 300$ km s $^{-1}$. The velocity dispersions of the protocluster galaxies are slightly larger on average but do not differ significantly from those in the field in our sample. The spatial extents and velocity dispersions of our sample are similar to those of the field galaxies at $z \sim 2$ with similar stellar mass (Erb et al. 2006b) but larger than those of LBGs at $z = 2 - 3$, which have half light radii $0''.1 - 0''.4$, corresponding to $0.8 \sim 3$ kpc, at rest-frame optical wavelength (e.g., Gavalisco et al. 1996; Akiyama et al. 2008) and $\sigma_v \lesssim 120$ km s $^{-1}$ measured with [OIII] $\lambda 5007$ (Pettini et al. 2001; Gnerucci et al. 2011, maybe biased to bright LBGs). This also supports that the *K*-selected members are the relatively massive galaxy population in the SSA22 protocluster, since [OIII] line widths and spatial extents depend on dynamical properties of gas and stellar components of galaxies.

4. DISCUSSION

Table 2
Summary of the targets

Classification	N _{targets}	N _{cluster} ^a	N _{field} ^b
All	67	24	15
$K < 24$ & $2.6 < z_{\text{phot}} < 3.6$	56	21	12
DRGs ($J - K > 1.4$)	21	11	4
HEROs ($J - K > 2.1$)	9	6	1
$24 \mu\text{m}$ sources	18	7	5
X-ray sources	14	4	4
LAEs	5(12) ^c	5(11) ^c	0

^aNumber of the galaxies confirmed the redshifts at $3.04 \leq z_{\text{spec}} \leq 3.12$.

^bNumber of the galaxies confirmed the redshifts at $z < 3.04$ and $z > 3.12$.

^cNumber of the LAEs selected with the narrow-band filter *NB497* which is sensitive to Ly α emission line at $z = 3.062 - 3.125$ (Hayashino et al. 2004; Yamada et al. 2012). The numbers in the brackets show the number of the galaxies with the *BV - NB497* color excess above 4σ significance.

4.1. The mass of the SSA22 protocluster

First, we discuss the mass of the SSA22 protocluster itself. Again, our NIR spectroscopic observations were conducted to cover the central highest density region of LAEs at $z = 3.09$ extended to $\sim 3 \times 6$ Mpc in physical scale (Yamada et al. 2012), which may evolve into a cluster core. Consequently, the region within 1.5 Mpc in physical (≈ 3.3 arcmin) from the density peak, indicated with the black large circle in Figure 1, was observed almost uniformly. This region is also uniformly covered with optical spectroscopic observations (Steidel et al. 2003; Lehmer et al. 2009b; Matsuda et al. 2005; Yamada et al. 2012). We here estimate the mass enclosed within this region. Note that the entire high density region of the SSA22 superstructure may extend to ~ 100 Mpc in the comoving scale (Yamada et al. 2012).

Figure 5 shows the redshift distributions of the protocluster galaxies within this region. The numbers of the galaxies at $3.04 \leq z_{\text{spec}} \leq 3.12$ within this radius are 18 for our sample, 45 for the sample confirmed with optical spectroscopic observations (Steidel et al. 2003; Lehmer et al. 2009b; Matsuda et al. 2005; Yamada et al. 2012) and 60 for the combined sample where we use our own redshifts for the overlapping objects. The redshift selection functions for LBGs and the photo-*z* selected galaxies are uniform at a redshift range from $z = 3.04$ to 3.12 while LAEs were nonuniformly selected in $z = 3.062 - 3.125$ and preferentially picked up around $z \approx 3.09$ due to the narrow-band selection shown in the *middle* panel of Figure 5.

It was reported that the redshift obtained with Ly α offsets for several 100 km s $^{-1}$ from the systemic one obtained with nebular emission lines (Steidel et al. 2010; Finkelstein et al. 2011; McLinden et al. 2011; Erb et al. 2014). It is thought that this offset of Ly α is caused by resonant scatterings in HI outflowing gas. The Ly α redshifts of our sample redshift by $40 \sim 640$ km s $^{-1}$ from our own [OIII] redshifts. We here ignore the offsets in the redshifts obtained with Ly α in calculating the velocity dispersion of the protocluster.

As seen in Figure 5, the galaxies in each sample are clearly clustered at the redshift ranges narrower than

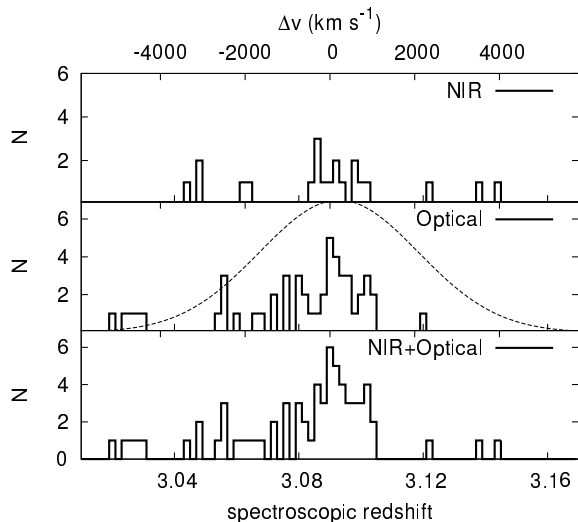


Figure 5. The redshift distributions of the galaxies within the central 1.5 Mpc of the SSA22 protocluster shown in Figure 1. The histograms show the redshift distributions of our sample (*top*), the galaxies confirmed the redshifts with optical spectroscopic observations in literatures (*middle*; based on Steidel et al. 2003; Lehmer et al. 2009b; Matsuda et al. 2005; Yamada et al. 2012) and the combined sample (*bottom*). The *top* axis shows the velocity scaled taking $z = 3.09$ as a center. The dashed curve in the *middle* panel shows the transmission curve of the NB497 filter, namely the selection function for LAEs at $z = 3.09$.

those expected from the redshift selection function of each sample. By fitting each of the redshift distributions at $3.04 \leq z \leq 3.12$ with a Gaussian profile, we obtain the velocity dispersions $\sigma_v = 521 \pm 122 \text{ km s}^{-1}$, $790 \pm 127 \text{ km s}^{-1}$ and $658 \pm 84 \text{ km s}^{-1}$ for the NIR, optical and combined samples, respectively. The centers of the redshift distributions are at $z = 3.091 \sim 3.092$ with the errors $\Delta z = 0.001 \sim 0.002$, agree well each other. If we simply evaluate the σ_v as the standard deviation of each redshift distribution at $3.04 \leq z \leq 3.12$, we obtain $\sigma_v = 1394, 1100$ and 1174 km s^{-1} for the NIR, optical and combined samples, respectively.

The velocity dispersions of our samples are similar to those of the protoclusters at $2 < z < 4$ obtained from LAEs by Venemans et al. (2007) but higher than those of $z = 3$ progenitors of massive clusters with $\sigma_v \sim 1000 \text{ km s}^{-1}$ in the local Universe, predicted from the numerical simulations (e.g., Eke et al. 1998). If we assume the virial equilibrium, the virial mass of this protocluster is $M_{\text{vir}} \sim 3\sigma_v^2 r / G = 4.5 \pm 1.1 \times 10^{14} M_{\odot}$ ($\sigma_v / 658 \text{ km s}^{-1}$) 2 ($r / 1.5 \text{ Mpc}$), where G is the gravitational constant.

It is, however, not likely to happen that the SSA22 protocluster has already been fully virialized. We then also evaluate the mass of the protocluster from its overdensity following Steidel et al. (1998) and Venemans et al. (2005). The mass of a protocluster with comoving volume V and mass overdensity δ_m , which is estimated from that of galaxies, is given as $M = \bar{\rho}V(1 + \delta_m)$ where $\bar{\rho}$ is the mean density of the Universe. The mean density $\bar{\rho}$ is $\approx 4.2 \times 10^{10} M_{\odot} \text{ Mpc}^{-3}$ at $z = 3.09$ for the cosmological parameters adopted in this paper. We here take the volume within the area same as that used to evaluate the velocity dispersion and the redshift range $3.08 < z < 3.10$ ($\approx 1500 \text{ km s}^{-1}$), which corresponds to $V \approx 2.2 \times 10^3$

Mpc^3 , as the comoving volume of the protocluster.

Overdensity of the galaxies in the protocluster is defined as the ratio of the number density of the galaxies in the protocluster (n_{cluster}), to that in the field (n_{field}) as $\delta_{\text{gal}} = (n_{\text{cluster}}/n_{\text{field}} - 1)$. We here estimate the overdensity from the fraction of the galaxies in the SSA22 protocluster among the targets with $K < 24$ and $2.6 < z_{\text{phot}} < 3.6$. Of the targets with $K < 24$ and $2.6 < z_{\text{phot}} < 3.6$ within the central 3.3 arcmin radius, 12 galaxies were confirmed at $3.08 < z < 3.10$ while the rest 32 galaxies were not confirmed at $3.04 \leq z \leq 3.12$. Assuming that the latter galaxies are the field galaxies within the redshift range of $2.6 < z < 3.6$, the overdensity of the galaxies in the SSA22 protocluster is estimated to be $\delta_{\text{gal}} = 17.8 \pm 5.4$. This is a lower limit value since not all the protocluster galaxies may be enough bright to be identified the redshifts by the detections of [OIII].

Following Steidel et al. (1998), the mass overdensity δ_m is related to the δ_{gal} as $1 + b\delta_m = C(1 + \delta_{\text{gal}})$, taking into account for the redshift space distortion caused by peculiar velocities. C can be approximated by $C = 1 + f - f(1 + \delta_m)^{1/3}$. f is the growth rate of the perturbations at the given redshift (Lahav et al. 1991), ~ 1 at $z > 2$ for the cosmology adopted here. Adopting the bias parameter $b = 3 \sim 5$ (e.g., Quadri et al. 2007; Ichikawa et al. 2007), we obtain the $\delta_m = 1.9 \sim 2.6$, which corresponds to the cluster mass of $1.8 \sim 2.4 \times 10^{14} M_{\odot}$.

Both methods found a cluster mass of several $10^{14} M_{\odot}$, suggesting that the mass of the SSA22 protocluster is already comparable to those of massive clusters in the local Universe. Such a massive halo at $z = 3$ is very rare, may be unique in the horizon, as predicted from the cosmological numerical simulations in the Λ CDM universe (e.g., Mo & White 2002). Since the SSA22 protocluster is an extremely outstanding structure at $z = 3$ as ever, it can happen that this protocluster is actually the one very rare cluster, although we should take carefully this result. We should note that our mass estimate is a conservative value since we adopt the volume including only the central part of the protocluster and its overdensity can be underestimated.

4.2. The red galaxies in the protocluster

Significant fractions of DRGs and HEROs in the SSA22 field were found to be the members of the protocluster. This spectroscopically supports our previous studies that reported the density excess of such red galaxies in the SSA22 protocluster (Uchimoto et al. 2012; Kubo et al. 2013).

We found that some of these red galaxies are quiescent galaxies which dominate the reddest color range. Of the six galaxies with $J - K \geq 2.4$ observed in this study, five were confirmed the redshifts at $z \approx 3.09$ while there are as a whole 13 such objects found in our photometric sample in the SSA22 field. Figure 6 shows examples of the SEDs of the protocluster galaxies with $J - K \geq 2.4$ and Figure 7 shows the stacked corresponding probability distributions of age, τ , dust extinction and metallicity parameters of all of them. Four galaxies are fitted with the $\chi^2/\nu < 0.84$ while the $\chi^2/\nu = 1.74$ for the rest one (J221737.3+001816.0, described in § 2) due to the large error of its rest-frame UV flux. They show quiescent star formation activities and are likely to be dominated

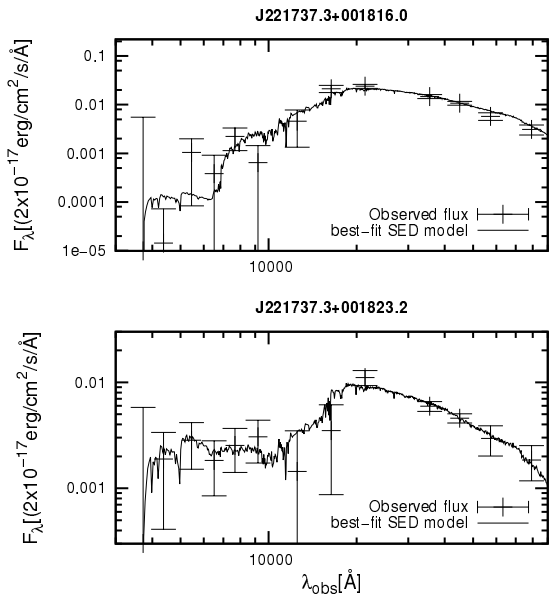


Figure 6. Examples of the SEDs of the massive quiescent galaxies confirmed in the SSA22 protocluster. The cross points are the observed flux values in the $u^*BVRI'z'JHK$, 3.6, 4.5, 5.8 and 8.0 μm -bands. The solid curves indicate their best-fit SED models. The best-fit SED models of J221737.3+001816.0 (*Top*) and J221737.3+001823.2 (*Bottom*) are those with $\text{SFR} \propto \exp(-t/\tau)$ where $\tau = 0.1$, $E(B-V)=0.1$, age = 2.0 Gyr and $Z = 0.2 Z_{\odot}$, and $\tau = 0.3$, $E(B-V)=0.1$, age = 0.7 Gyr and $Z = 0.4 Z_{\odot}$, respectively.

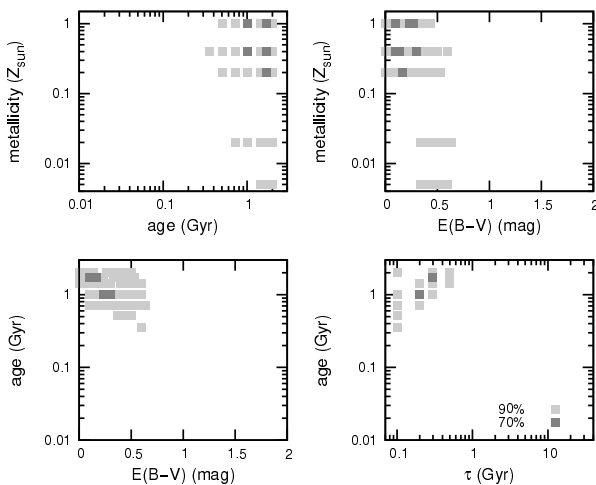


Figure 7. The stacked probability distributions of age, metallicity, τ and $E(B-V)$ parameters of all the protocluster galaxies with $J-K > 2.4$. The dark gray and gray shaded areas show the 70% and 90% confidence regions, respectively.

by old stellar populations while their best-fit SED parameters are $\tau = 0.1 - 0.3$ Gyr, age = 0.7 – 2.0 Gyr, $Z = 0.2 - 1 Z_{\odot}$, $M_{\text{star}} = 10^{10.9} - 10^{11.5} M_{\odot}$ and specific SFR (sSFR) $< 0.1 \text{ Gyr}^{-1}$. As for the SED models within the 70% confidence range of the stacked probability distribution, more than 90% of stars in an object are older than 0.7 Gyr. Although the SED models within the 90% confidence range have the ages ranging from 0.3 to 2.0 Gyr, their sSFR are smaller than 0.4 Gyr^{-1} . As we describe below, four of them are AGNs detected with *Chandra*. The origin of their [OIII] $\lambda 5007$ emission lines

should be AGNs but there is no AGN feature in their rest-frame UV to NIR SEDs. They may be buried in the stellar light as is often the case for AGNs at high redshift (e.g., Yamada et al. 2009). The other one without *Chandra* detection is J221737.3+001816.0, confirmed from the Balmer and 4000Å breaks. High AGN fractions in massive quiescent galaxies at $z = 2 - 3$ were also reported in other studies (e.g., Tanaka et al. 2013; Straatman et al. 2014).

From these above, they are well-characterized as massive galaxies with quenched star formation. This may be the first time to confirm the association of a bunch of massive quiescent galaxies in a protocluster at $z > 3$, spectroscopically. This also confirms our previous results that reported the overdensity of massive quiescent galaxies in the SSA22 protocluster selected based on the photometric redshifts and the color selections (Kubo et al. 2013). They are very likely to take a part of progenitors of massive early-type galaxies at cores of massive clusters in the current Universe.

Of the five quiescent galaxies, four are AGNs detected with *Chandra*. Their X-ray luminosities at 2 – 10 keV evaluated from their hard band (2 – 8 keV) flux values assuming the spectra in form $f_{\nu} \sim \nu^{-0.7}$ are $L_X \sim 3 - 7 \times 10^{43} \text{ ergs s}^{-1}$. They have the X-ray luminosities lower than those of the other X-ray sources associated with LAEs and LBGs in the SSA22 protocluster (Lehmer et al. 2009a). Specific AGN activities, X-ray luminosities divided with stellar masses of host galaxies, of them are $L_X/M_{\text{star}} = 3 - 8 \times 10^{32} (\text{erg s}^{-1} M_{\odot}^{-1})$, calculated following Yamada et al. (2009). These values are similar to or slightly higher than those of local massive galaxies, if we assume the similar black hole to stellar mass ratio. It suggests that the massive quiescent galaxies in the SSA22 protocluster may be at the phase after the peaks of not only the star formation activities but also the mass accretion into their central black holes. We can consider two scenarios for the declines of both the activities; quench of mass accretion to the central black holes due to exhaustion of the gas by star formation and/or quench of star formation by feedback from the AGNs. The latter is an important scenario in the recent cosmological numerical simulations since this may solve the over cooling problem at the high-mass end (e.g., Croton et al. 2005; Bower et al. 2006).

We also identified the six DRGs with $1.4 < J-K < 2.4$ as the protocluster members. They are too faint to constrain the robust SED properties but their [OIII] $\lambda 5007$ may be originated in the star formation activities since there is no significant AGN feature. At least, one of them is likely to be a heavily dust obscured galaxy since it is detected at 24 μm and also located within the beam size of an 1.1-mm source, AzTEC 99 (Umeahata et al. 2014).

4.3. Emission line properties

As we reported in § 3, there is no significant difference in widths and spatial extents of emission lines between the K -selected galaxies in the protocluster and field whereas their other properties distinctly differ from those of rest-frame UV selected galaxies such as LAEs and LBGs.

Figure 8 shows the [OIII] $\lambda 5007/\text{H}\beta$ line flux ratio versus stellar mass distribution, called Mass Excitation

(MEx) diagram (Juneau et al. 2011), of our sample. Lower limit values of the $[\text{OIII}] \lambda 5007/\text{H}\beta$ ratios are shown for the galaxies without detection of $\text{H}\beta$. The blue square shows the stacked value of all the galaxies confirmed by the detections of $[\text{OIII}] \lambda 5007$ but without detections of $\text{H}\beta$. $[\text{OIII}] \lambda 5007/\text{H}\beta$ ratios obtained with the $HK500$ grism are not shown since they are contaminated by OH airglow lines. We also plot the star-forming galaxies and AGNs in the SDSS catalog (using the catalog provided by Tremonti et al. 2004) and the LBGs at $z \sim 3$ studied by Maiolino et al. (2008) and Mannucci et al. (2009) for comparison.

$[\text{OIII}] \lambda 5007/\text{H}\beta$ ratios of galaxies at $z = 2 - 3$ are typically higher than those of local star-forming galaxies (e.g., Erb et al. 2006a; Maiolino et al. 2008; Mannucci et al. 2009; Trump et al. 2011). It is thought to originate in high SFRs and low metallicities of high redshift galaxies. An AGN can also enhance $[\text{OIII}] \lambda 5007/\text{H}\beta$ ratio but it may not be so common as found from the emission line diagnostics of $z \sim 2$ galaxies (e.g., Erb et al. 2006a). The galaxies in our sample show large $[\text{OIII}] \lambda 5007/\text{H}\beta$ ratios on average, similar to LBGs at $z \sim 3$. The AGNs in the protocluster show large $[\text{OIII}] \lambda 5007/\text{H}\beta$ ratios and stellar masses similar to those of local AGNs and also AGNs at $z \sim 1$ (Juneau et al. 2011).

One counterpart of LAB01 has $\text{Log}([\text{OIII}] \lambda 5007/\text{H}\beta) = 0.21^{+0.29}_{-0.06}$, which is lower than those of other star-forming galaxies at $z \sim 3$. This galaxy is an active starburst galaxy detected at $24 \mu\text{m}$ and its SED is well-fitted with a dusty starburst galaxy model. Then its ionizing radiation field may be similar to or harder than those of other star-forming galaxies. One possible interpretation is that this galaxy has reached the level of chemical enrichment of galaxies in the local Universe, as $[\text{OIII}]/\text{H}\beta$ ratio depends on metallicity at the given ionization parameter. The difference in the chemical enrichment in the protocluster was reported in Kulas et al. (2013) that the galaxies in the protocluster at $z \sim 2$ have various metallicities regardless of the stellar masses whereas field galaxies follow the well-established trend in the mass-metallicity relation at that epoch. At this point, it is hard to constrain the metallicities of the protocluster galaxies based on our spectroscopic data and also SED fittings of the photometric data. Further spectroscopic observations for $[\text{OII}] \lambda 3727$ emission lines are required to constrain the metallicities of the galaxies in the SSA22 protocluster.

5. CONCLUSION

We conducted NIR spectroscopy of the rest-frame optically-selected candidate members of the protocluster at $z = 3.09$ in the SSA22 field. We observed the 67 candidates and confirmed the redshifts of the 39 galaxies. We identified the 24 protocluster galaxies at $3.04 \leq z_{\text{spec}} \leq 3.12$ which are on average more massive than those identified by the previous observations in rest-frame UV. This may be one of the first observations to confirm a large number of galaxies at $z \sim 3$ from the redshifted $[\text{OIII}] \lambda 5007$ emission lines. We also found that notable fractions of DRGs, HEROs, $24 \mu\text{m}$ sources, AGNs, and the counterparts of LABs and the AzTEC/ASTE 1.1-mm sources in the SSA22 field are the members of the protocluster at $z = 3.09$.

The mass of the SSA22 protocluster was evaluated to

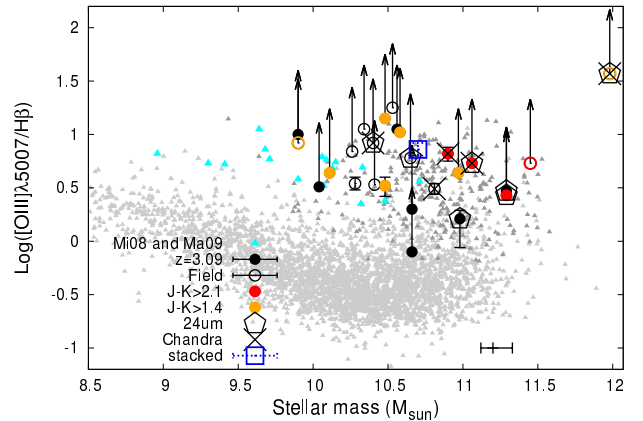


Figure 8. $[\text{OIII}] \lambda 5007/\text{H}\beta$ ratio versus stellar mass diagram of our sample. The filled circles show the galaxies at $3.04 \leq z_{\text{spec}} \leq 3.12$ and the blank circles show the field galaxies at $2.9 < z_{\text{spec}} < 3.4$ in our sample. The galaxies classified as $J - K \leq 1.4$, $1.4 < J - K \leq 2.1$ and $J - K < 2.1$, are shown with the black, orange and red points, respectively. The blue square shows the stacked value of the galaxies confirmed by the detections of $[\text{OIII}] \lambda 5007$ but without detections of $\text{H}\beta$ in our sample. The large pentagons and crosses mark the $24 \mu\text{m}$ and X-ray sources, respectively. The light and dark gray points show the galaxies and AGNs in the SDSS catalog (Tremonti et al. 2004). The cyan triangles show the LBGs at $z \sim 3$ (Maiolino et al. 2008; Mannucci et al. 2009).

be $2 \sim 5 \times 10^{14} M_{\odot}$. This structure is very likely to be one progenitor of the most massive clusters in the current Universe.

We also confirmed the presence of massive quiescent galaxies in the SSA22 protocluster. It supports the early formation of massive early-type galaxies in such high density region. Most of them are also detected in X-ray, suggesting that AGNs play an important role in the formation history of massive early-type galaxies.

This study is based on data collected at Subaru Telescope, which is operated by the National Astronomical Observatory of Japan. We would like to thank the Subaru Telescope staff for many help and support for the observations. Our studies owe a lot deal to the archival Subaru Suprime-Cam (Matsuda et al. 2004), *Spitzer* IRAC & MIPS data taken in Webb et al. (2009), *Chandra* data taken in Lehmer et al. (2009a). We also thank to AzTEC/ASTE observers of the SSA22 field providing the updated source catalog. This work was supported by Global COE Program "Weaving Science Web beyond Particle-Matter Hierarchy", MEXT, Japan. YM acknowledges support from JSPS KAKENHI Grant Number 20647268. This work was partially supported by JSPS Grants-in-Aid for Scientific Research No.26400217.

Funding for the SDSS and SDSS-II has been provided by the Alfred P. Sloan Foundation, the Participating Institutions, the National Science Foundation, the U.S. Department of Energy, the National Aeronautics and Space Administration, the Japanese Monbukagakusho, the Max Planck Society, and the Higher Education Funding Council for England. The SDSS Web Site is <http://www.sdss.org/>. The SDSS is managed by the Astrophysical Research Consortium for the Participating Institutions. The Participating Institutions are

the American Museum of Natural History, Astrophysical Institute Potsdam, University of Basel, University of Cambridge, Case Western Reserve University, University of Chicago, Drexel University, Fermilab, the Institute for Advanced Study, the Japan Participation Group, Johns Hopkins University, the Joint Institute for Nuclear Astrophysics, the Kavli Institute for Particle Astrophysics and Cosmology, the Korean Scientist Group, the Chinese Academy of Sciences, Los Alamos National Laboratory, the Max-Planck-Institute for Astronomy, the Max-Planck-Institute for Astrophysics, New Mexico State University, Ohio State University, University of Pittsburgh, University of Portsmouth, Princeton University, the United States Naval Observatory, and the University of Washington.

REFERENCES

- Akiyama, M., Minowa, Y., Kobayashi, N., et al. 2008, *ApJS*, 175, 1
- Bertin, E., & Arnouts, S. 1996, *A&AS*, 117, 393
- Bower, R. G., Benson, A. J., Malbon, R., et al. 2006, *MNRAS*, 370, 645
- Bower, R. G., Lucey, J. R., & Ellis, R. S. 1992, *MNRAS*, 254, 601
- Bruzual, G., & Charlot, S. 2003, *MNRAS*, 344, 1000
- Calzetti, D., Armus, L., Bohlin, R. C., et al. 2000, *ApJ*, 533, 682
- Caputi, K. I., Dunlop, J. S., McLure, R. J., et al. 2012, *ApJ*, 750, L20
- Chabrier, G. 2003, *PASP*, 115, 763
- Croton, D. J., Farrar, G. R., Norberg, P., et al. 2005, *MNRAS*, 356, 1155
- Daddi, E., Alexander, D. M., Dickinson, M., et al. 2007, *ApJ*, 670, 173
- Ebizuka, N., Ichiyama, K., Yamada, T., et al. 2011, *PASJ*, 63, 605
- Eke, V. R., Navarro, J. F., & Frenk, C. S. 1998, *ApJ*, 503, 569
- Ellis, R. S., Smail, I., Dressler, A., et al. 1997, *ApJ*, 483, 582
- Erb, D. K., Shapley, A. E., Pettini, M., et al. 2006a, *ApJ*, 644, 813
- Erb, D. K., Steidel, C. C., Shapley, A. E., et al. 2006b, *ApJ*, 646, 107
- Erb, D. K., Steidel, C. C., Trainor, R. F., et al. 2014, *ApJ*, 795, 33
- Fassbender, R., Nastasi, A., Böhringer, H., et al. 2011, *A&A*, 527, L10
- Finkelstein, S. L., Hill, G. J., Gebhardt, K., et al. 2011, *ApJ*, 729, 140
- Franx, M., Labbé, I., Rudnick, G., et al. 2003, *ApJ*, 587, L79
- Gialalisco, M., Steidel, C. C., & Macchetto, F. D. 1996, *ApJ*, 470, 189
- Gnerucci, A., Marconi, A., Cresci, G., et al. 2011, *A&A*, 528, A88
- Gobat, R., Daddi, E., Onodera, M., et al. 2011, *A&A*, 526, A133
- Gobat, R., Strazzullo, V., Daddi, E., et al. 2012, *ApJ*, 759, L44
- Hayashino, T., Matsuda, Y., Tamura, H., et al. 2004, *AJ*, 128, 2073
- Ichikawa, T., Suzuki, R., Tokoku, C., et al. 2007, *PASJ*, 59, 1081
- Ilbert, O., McCracken, H. J., Le Fèvre, O., et al. 2013, *A&A*, 556, A55
- Juneau, S., Dickinson, M., Alexander, D. M., & Salim, S. 2011, *ApJ*, 736, 104
- Kodama, T., Tanaka, I., Kajisawa, M., et al. 2007, *MNRAS*, 377, 1717
- Kriss, G. 1994, *Astronomical Data Analysis Software and Systems*, 3, 437
- Kubo, M., Uchimoto, Y. K., Yamada, T., et al. 2013, *ApJ*, 778, 170
- Kulas, K. R., McLean, I. S., Shapley, A. E., et al. 2013, *ApJ*, 774, 130
- Lahav, O., Lilje, P. B., Primack, J. R., & Rees, M. J. 1991, *MNRAS*, 251, 128
- Lehmer, B. D., Alexander, D. M., Geach, J. E., et al. 2009a, *ApJ*, 691, 687
- Lehmer, B. D., Alexander, D. M., Chapman, S. C., et al. 2009b, *MNRAS*, 400, 299
- Maiolino, R., Nagao, T., Grazian, A., et al. 2008, *A&A*, 488, 463
- Mannucci, F., Cresci, G., Maiolino, R., et al. 2009, *MNRAS*, 398, 1915
- Marsan, Z. C., Marchesini, D., Brammer, G. B., et al. 2014, *ArXiv e-prints*
- Matsuda, Y., Yamada, T., Hayashino, T., et al. 2004, *AJ*, 128, 569
- , 2005, *ApJ*, 634, L125
- Matsuda, Y., Smail, I., Geach, J. E., et al. 2011, *MNRAS*, 416, 2041
- McLinden, E. M., Finkelstein, S. L., Rhoads, J. E., et al. 2011, *ApJ*, 730, 136
- Meza, A., Navarro, J. F., Steinmetz, M., & Eke, V. R. 2003, *ApJ*, 590, 619
- Mo, H. J., & White, S. D. M. 2002, *MNRAS*, 336, 112
- Mullis, C. R., Rosati, P., Lamer, G., et al. 2005, *ApJ*, 623, L85
- Muzzin, A., Marchesini, D., Stefanon, M., et al. 2013, *ApJ*, 777, 18
- Naab, T., Johansson, P. H., Ostriker, J. P., & Efstathiou, G. 2007, *ApJ*, 658, 710
- Oser, L., Ostriker, J. P., Naab, T., Johansson, P. H., & Burkert, A. 2010, *ApJ*, 725, 2312
- Ouchi, M., Shimasaku, K., Akiyama, M., et al. 2005, *ApJ*, 620, L1
- Papovich, C., Dickinson, M., & Ferguson, H. C. 2001, *ApJ*, 559, 620
- Pettini, M., Shapley, A. E., Steidel, C. C., et al. 2001, *ApJ*, 554, 981
- Quadri, R., van Dokkum, P., Gawiser, E., et al. 2007, *ApJ*, 654, 138
- Salpeter, E. E. 1955, *ApJ*, 121, 161
- Shapley, A. E., Steidel, C. C., Adelberger, K. L., et al. 2001, *ApJ*, 562, 95
- Shapley, A. E., Steidel, C. C., Pettini, M., Adelberger, K. L., & Erb, D. K. 2006, *ApJ*, 651, 688
- Skrutskie, M. F., Cutri, R. M., Stiening, R., et al. 2006, *AJ*, 131, 1163
- Stanford, S. A., Eisenhardt, P. R., & Dickinson, M. 1998, *ApJ*, 492, 461
- Steidel, C. C., Adelberger, K. L., Dickinson, M., et al. 1998, *ApJ*, 492, 428
- Steidel, C. C., Adelberger, K. L., Shapley, A. E., et al. 2000, *ApJ*, 532, 170
- , 2003, *ApJ*, 592, 728
- Steidel, C. C., Erb, D. K., Shapley, A. E., et al. 2010, *ApJ*, 717, 289
- Straatman, C. M. S., Labbé, I., Spitler, L. R., et al. 2014, *ApJ*, 783, L14
- Tamura, Y., Kohno, K., Nakanishi, K., et al. 2009, *Nature*, 459, 61
- Tanaka, M., Finoguenov, A., Mirkazemi, M., et al. 2013, *PASJ*, 65, 17
- Toshikawa, J., Kashikawa, N., Ota, K., et al. 2012, *ApJ*, 750, 137
- Totani, T., Yoshii, Y., Iwamuro, F., Maihara, T., & Motohara, K. 2001, *ApJ*, 558, L87
- Tremonti, C. A., Heckman, T. M., Kauffmann, G., et al. 2004, *ApJ*, 613, 898
- Trump, J. R., Weiner, B. J., Scarlata, C., et al. 2011, *ApJ*, 743, 144
- Uchimoto, Y. K., Suzuki, R., Tokoku, C., et al. 2008, *PASJ*, 60, 683
- Uchimoto, Y. K., Yamada, T., Kajisawa, M., et al. 2012, *ApJ*, 750, 116
- Umehata, H., Tamura, Y., Kohno, K., et al. 2014, *MNRAS*, 440, 3462
- Venemans, B. P., Röttgering, H. J. A., Miley, G. K., et al. 2005, *A&A*, 431, 793
- , 2007, *A&A*, 461, 823
- Visvanathan, N., & Sandage, A. 1977, *ApJ*, 216, 214
- Webb, T. M. A., Yamada, T., Huang, J.-S., et al. 2009, *ApJ*, 692, 1561
- Yamada, T., Nakamura, Y., Matsuda, Y., et al. 2012, *AJ*, 143, 79
- Yamada, T., Kajisawa, M., Akiyama, M., et al. 2009, *ApJ*, 699, 1354
- Yoshikawa, T., Akiyama, M., Kajisawa, M., et al. 2010, *ApJ*, 718, 112

Table 3
Catalog of the galaxies confirmed by our NIR spectroscopic observations

ID	grism	K_s^a (mag)	$J - K^b$ (mag)	z_{lit}^c	Detected Lines	z_{spec}	Flux ^d (10^{-17} ergs s $^{-1}$ cm $^{-2}$)	M_{star} ($10^{10} M_{\odot}$)	note
J221718.0+001735.6	VPH-K	23.5	1.1	!D	[OIII] 5007	3.1423 ± 0.0003	12.4 ± 0.6	$2.8^{+1.2}_{-0.5}$...
J221719.4+001657.1	VPH-K	23.2	1.4	!D	[OIII] 4959, 5007	3.3082 ± 0.0001	5.8 ± 0.3	$0.8^{+2.2}_{-0.1}$...
J221716.4+001718.6	VPH-K	23.1	0.8	!D	[OIII] 5007	3.3552 ± 0.0001	5.8 ± 0.4	$2.5^{+1.0}_{-0.4}$...
J221715.7+001906.2	VPH-K	> 25.2	...	3.1015	[OIII] 5007	3.1008 ± 0.0001	2.0 ± 0.3	$0.2^{+0.3}_{-0.1}$	Y12
J221726.1+001232.3	VPH-K	22.1	1.3	!D	H β , [OIII] 4959, 5007	3.1000 ± 0.0003	13.8 ± 1.4	$9.5^{+7.5}_{-2.5}$	LAB01 ^e
J221725.7+001238.7	VPH-K	23.6	0.3	...	[OIII] 4959, 5007	3.1007 ± 0.0002	2.0 ± 0.3	$1.1^{+0.6}_{-0.3}$	LAB01 ^e
J221724.9+001117.5	VPH-K	23.1	0.8	...	[OIII] 5007	3.0689 ± 0.0002	4.2 ± 0.4	$4.1^{+0.5}_{-2.0}$	LAB16 ^e
J221732.5+001131.2	VPH-K	23.4	0.4	3.0767 (3.0677)	[OIII] 5007	3.0680 ± 0.0003	1.7 ± 0.3^f	$4.4^{+0.2}_{-0.3}$	LAB30 ^e , S06 (S06)
J221732.5+001132.8	VPH-K	23.0	0.9	3.0716 (3.0649)	[OIII] 5007	3.0687 ± 0.0004	0.7 ± 0.2^f	$4.2^{+0.2}_{-0.6}$	LAB30 ^e , S06 (S06)
J221733.9+001106.5	VPH-K	22.5	1.0	...	[OIII] 5007	2.8596 ± 0.0001	3.9 ± 0.4	$4.5^{+5.3}_{-1.1}$...
J221730.2+001120.7	VPH-K	20.9	0.8	...	[OIII] 5007	3.0667 ± 0.0002	3.8 ± 0.3	$19.4^{+0.0}_{-0.0}$...
J221720.8+001831.0	HK500	20.4	1.4	2.840	[OIII] 5007	2.9054 ± 0.0007	31.9 ± 1.6	$95.1^{+0.0}_{-18.9}$	L09
J221726.3+001957.2	HK500	23.2	1.8	...	[OIII] 5007	3.0431 ± 0.0006	11.5 ± 1.2	$3.0^{+3.1}_{-1.2}$...
J221724.8+001803.7	HK500	22.3	2.5	...	[OIII] 5007	3.3868 ± 0.0010^g	3.8 ± 1.9	$28.4^{+35.0}_{-9.2}$...
J221727.0+001746.4	HK500	23.2	0.9	...	[OIII] 5007	3.3235 ± 0.0004	4.9 ± 0.5	$1.8^{+0.4}_{-0.9}$...
J221728.5+001807.4	HK500	23.0	0.9	...	[OII] 3726	3.4281 ± 0.0012	9.1 ± 2.2	$6.3^{+1.1}_{-1.4}$...
J221727.3+001809.5	HK500	22.7	1.2	3.091(3.0855)	H β , [OIII] 4959, 5007	3.0861 ± 0.0009	10.3 ± 2.3	$2.0^{+0.7}_{-0.8}$	S03 (P01)
J221734.9+001911.8	HK500	23.3	1.2	...	[OIII] 5007	3.0609 ± 0.0010	6.8 ± 1.3	$0.8^{+1.4}_{-0.3}$...
J221737.3+001823.2	VPH-K	22.5	2.8	...	H β , [OIII] 4959, 5007	3.0851 ± 0.0001	19.1 ± 0.7	$8.0^{+5.7}_{-2.9}$	AzTEC14 ^{h,i}
J221736.8+001818.2	VPH-K	23.1	1.6	...	[OIII] 4959, 5007	3.0926 ± 0.0003	6.5 ± 0.8
J221737.3+001816.0	HK500	21.6	2.8	...	[OIII] 5007	3.0854 ± 0.0003	2.8 ± 0.4	$9.3^{+19.7}_{-5.0}$	AzTEC14 ^h
J221737.0+001820.4	VPH-K	22.8	0.4	...	P β	0.5763 ± 0.0002	3.6 ± 1.0	$25.4^{+7.3}_{-5.8}$	AzTEC14 ^h
J221732.0+001655.5	VPH-K	22.2	2.6	...	[OIII] 5007	3.0909 ± 0.0004	2.8 ± 0.7	$0.3^{+0.0}_{-0.0}$	AzTEC14 ^h
J221736.5+001622.6	VPH-K	20.4	0.5	3.084	[OIII] 5007	3.0945 ± 0.0008	2.1 ± 3.5	$11.5^{+23.9}_{-4.9}$	LAB12 ^e
J221731.8+001606.3	VPH-K	23.0	1.7	...	H β , [OIII] 5007	3.0981 ± 0.0002	11.3 ± 0.8	$11.8^{+0.0}_{-0.0}$	S03
J221737.1+001712.4	VPH-K	23.5	1.1	...	[OIII] 5007	3.0899 ± 0.0004	7.2 ± 0.9	$3.0^{+3.2}_{-1.5}$...
J221732.2+001502.3	VPH-K	22.8	1.8	...	[NII] 6584, H α	2.3252 ± 0.0002	8.7 ± 1.7	$3.6^{+8.6}_{-0.8}$...
J221737.3+001630.7	VPH-K	22.0	2.4	...	[OIII] 5007	3.0888 ± 0.0004	6.1 ± 0.8	$12.5^{+2.3}_{-5.0}$...
J221727.8+001736.6	HK500	23.7	1.8	3.0922	[OIII] 5007	3.0916 ± 0.0012	4.0 ± 2.2	$8.1^{+1.3}_{-0.0}$...
J221729.6+001918.6	HK500	23.6	1.8	3.102	[OIII] 4959 ^k	3.1021 ± 0.0024	3.2 ± 2.5	$3.9^{+0.9}_{-2.0}$	Y12
J221728.3+001954.4	HK500	22.6	0.6	...	H β , [OIII] 4959, 5007	3.1019 ± 0.0005	6.1 ± 1.6	$1.3^{+2.1}_{-0.3}$	Y12
J221728.5+001822.2	HK500	23.0	0.5	...	[OIII] 5007	3.3148 ± 0.0004	7.8 ± 0.6	$4.1^{+2.5}_{-0.7}$...
J221729.7+001715.2	HK500	22.7	0.5	...	[OIII] 5007	3.1390 ± 0.0056	4.2 ± 3.9	$2.2^{+0.0}_{-0.0}$...
J221725.4+001716.9	VPH-K	21.7	2.4	3.120	H β	3.0482 ± 0.0003	5.6 ± 0.6	$4.5^{+1.2}_{-0.0}$...
J221725.2+001805.7	VPH-K	22.7	2.2	...	[OIII] 5007	3.0973 ± 0.0004	1.7 ± 0.4	$11.2^{+1.5}_{-2.1}$	(LAB35) ^e , L09
J221722.3+001640.1	VPH-K	20.5	0.3	3.360 (3.353)	H β , [OIII] 4959, 5007	3.3544 ± 0.0001	39.0 ± 1.4	$17.2^{+27.8}_{-1.9}$	AzTEC99 ^h
								$6.5^{+0.0}_{-0.0}$	S03 (S03)

Table 3
Continued

ID	grism	K_s^a (mag)	$J - K^b$ (mag)	z_{lit}^c	Detected Lines	z_{spec}	Flux ^d (10^{-17} ergs s $^{-1}$ cm $^{-2}$)	M_{star} ($10^{10} M_{\odot}$)	note
J221721.9+001755.5	VPH- <i>K</i>	22.9	0.9	...	H β , [OIII] 4959, 5007	3.4075 ± 0.0001	11.3 ± 0.4	$1.9^{+0.9}_{-1.1}$...
J221724.3+001945.1	VPH- <i>K</i>	22.6	0.3	...	[OIII] 5007	3.1211 ± 0.0003	2.4 ± 0.4	$2.6^{+0.5}_{-0.1}$...
J221724.6+001836.5	VPH- <i>K</i>	21.9	0.6	...	[OIII] 5007	3.0847 ± 0.0006	2.3 ± 0.5	$7.5^{+1.5}_{-0.3}$...

^aTotal magnitudes, MAG_AUTO estimated by SExtractor (Bertin & Arnouts 1996) on the K_s -band images.

^b $J - K$ colors measured in $1''.1$ apertures centered at the coordinates on the K -band images.

^cThe spectroscopic redshifts in literatures. The references of the spectroscopic redshifts are shown in the notes as follows; Pettini et al. (2001) (P01); Steidel et al. (2003) (S03); Shapley et al. (2006) (S06) Lehmer et al. (2009b) (L09); Yamada et al. (2012) (Y12). z_{lit} cited from S03, S06 and Y12 were identified with Ly α while those identified with absorption features are also written in the brackets of J221732.5+001131.2, J221732.5+001132.8 and J221722.3+001640.1. z_{lit} cited from L09 were measured with optical spectroscopic observations. z_{lit} cited from P01 (in the bracket of J221727.3+001809.5) was identified with nebular emission lines obtained with NIR spectroscopy.

^dFlux values of the strongest emission lines. The flux values of [OIII] λ 5007 or H α are shown for the objects detected of more than one emission lines.

^eThe counterparts of LABs at $z = 3.09$ (Matsuda et al. 2004). J221725.4+001716.9 is not located within but very close to LAB35.

^fThe flux values of J221732.5+001131.2 and J221732.5+001132.8 may be underestimated. Since they were observed within the same slit and located very close, their signals were subtracted by each other in the sky subtraction. And also, to acquire the both objects, we put the slit slightly off the center of J221732.5+001132.8. Actually, the flux of J221732.5+001132.8 is smaller than that obtained by Erb et al. (2014).

^gThe emission line is not likely to originate in this bright object since it was detected at slightly below the position of the faint continuum emission which may be originated in this bright object.

^hThe counterparts of the AzTEC/ASTE 1.1-mm sources (Umehata et al. 2014).

ⁱShowing a line profile with double peaks.

^jConfirmed from the Balmer and 4000 \AA breaks in its continuum spectrum (described in § 2).

^kWe interpreted this emission line as [OIII] λ 4959 since the offset from z_{lit} become much larger if we interpret this line as [OIII] λ 5007. The wavelength where its [OIII] λ 5007 is expected from the z_{lit} is buried by crowded OH airglow lines.